Experiments on Nonlinear Harmonic Wave Generation from Colliding Internal Wave Beams

S.Smith[a], J. Crockett[a,*]

[a]Department of Mechanical Engineering, Brigham Young Univeristy, Provo, Utah 84602, USA

Abstract

Internal waves are abundant in both the ocean and atmosphere. However, nonlinear generation of harmonic waves due to interactions between internal waves have not been a major focus in previous research. When two nonresonant internal waves collide, harmonics are formed at the sum and difference of multiples of the colliding waves' frequencies, taking energy from the initial wave beams. Here we experimentally create interactions between nonresonant internal waves and determine a relative energy partition to second-harmonics for eight unique configurations. It is found that approximately 6% to 19% of the original relative energy of the two interacting waves is partitioned to harmonics. It is found that this value is more dependent on the relative direction of the colliding waves approach to each other than on their particular frequencies. The majority of the incoming energy from the colliding waves also leaves the interaction with the same frequency.

Keywords: internal wave, stratification, harmonic waves, nonlinear

1. Introduction

Internal waves are consistently generated in continuous, stably stratified fluids, such as the ocean and atmosphere. In these media the density of the fluid increases continually with depth, due to salinity and temperature (ocean) or just temperature (atmosphere). As this stable stratification is disturbed, fluid particles are moved to regions where they are no longer neutrally buoyant, and will begin to oscillate. These motions generate internal waves. In recent decades, it has been found that internal waves have a non-negligible effect on the transfer and dissipation of energy in both the atmosphere and ocean [1]. The energy transferred by internal waves contributes to sustaining deep ocean life through ocean mixing [2, 3] and can affect global climate patterns [4] through altering the global energy distribution. A greater understanding of how internal waves are generated, interact with surrounding phenomena, and dissipate aids in understanding how internal wave energy transfer affects the global energy distribution. Simplified linear models have been used extensively to estimate the generation, propagation, and dissipation of internal waves. Unfortunately, nonlinear

*Corresponding author
Email addresses: sean.smith1121@gmail.com (S.Smith), crockettj@byu.edu (J. Crockett)

effects can make significant contributions to energy exchange among internal waves and much is still to be learned in this area.

In an attempt to capture the nonlinear dynamics of interenal wave propagation multiple studies have focused on internal waves interacting with realistic phenomena. These include wave propagation through vorticies [5, 6], shear [7–11], density discontinuities [12–14], sheared denisity variations [15], solid boundaries [16, 17], and other internal waves [18–23]. When these interactions are nonlinear complexities are introduced and often harmonic wave generation occurs. Thorpe created an analytical model of nonlinear wave reflection at a density interface and found harmonics generated at twice the original wave frequency [13]. Higher harmonics were also found during reflection from a sloping solid surface in numerical models [24], experiments [25, 26], and ocean observations [27].

A particular type of wave-wave interaction which has been studied extensively is a resonant wave-wave interaction. In this situation two internal waves of nearly the same spatial and temporal scales collide and all of their energy is transferred to a third wave such that $\omega_1 \pm \omega_2 = \omega_3$ and $\mathbf{k_1} \pm \mathbf{k_2} = \mathbf{k_3}$ where ω is the wave frequency and $\mathbf{k}$ is the total wavenumber. The frequency, ω, satisfies the dispersion relation,

$$\omega^2 = \mathrm{N}^2 \frac{k^2}{k^2 + l^2}, \tag{1}$$

where k and l are the horizontal and vertical wavenumbers, and N is the Brunt-Väisälä frequency defined as

$$N^2 = \frac{g}{\rho_0} \frac{\partial \bar{\rho}}{\partial z}. \tag{2}$$

Internal waves only exist at frequencies less than that of the buoyancy frequency.

Resonant wave-wave interactions were first believed to be important when introduced by Phillips [28]. They have since been the focus of many studies [29–32] which have shown their significant contribution to energy transfer between frequencies in the Garrett and Munk spectrum [33]. Despite the prevalence of studies on resonant wave-wave interactions, there have been relatively few studies concerning nonresonant wave-wave interactions. These are wave-wave interactions which do not conform to the resonance condition, however waves of harmonic frequencies may be generated due to the nonlinear collision of the waves.

As with resonant wave-wave interactions, when two nonresonant internal waves collide, harmonics at the sum and difference of multiples of the colliding waves' frequencies are formed. This phenomena is can be characterized by

$$\omega_{harmonic} = \mid \mathrm{A}\omega_1 \pm \mathrm{B}\omega_2 \mid, \tag{3}$$

where ω_i represents the frequencies of the colliding waves ($i = 1, 2$), and A and B represent any integer. Lower order harmonics, where A and B are small, are generally more important than higher order harmonics, and only harmonics with frequencies less than the Brunt-Väisälä frequency of the fluid can develop into propagating internal waves. In order for these harmonics to form, energy must be transferred from the colliding waves to the harmonics. However, unlike resonant wave-wave interactions, colliding nonresonant internal waves only partition a portion of their energy to generated harmonics. To the author's knowledge, no previously performed laboratory experiments have attempted to quantify the partition of energy from the colliding internal waves to generated harmonics.

A nonresonant wave-wave interaction was created by McEwan [34] as he explored the impact of interactions on the continuous stratification of the fluid, but there was little focus on generated harmonics. Chashechkin and Neklyudov [35] found harmonic frequencies present in their experiments by inserting conductivity probes in and around the interaction region of two colliding waves. They found the amplitudes of the generated harmonics but did not quantify the energy partitioned to the harmonics. Internal wave interactions were visualized by Teoh et al. [36], but no harmonic internal waves were reported in this case due to symmetry and the harmonic frequencies being higher than the Brunt-Väisälä frequency. Instead, energy accumulated in the evanescent harmonics until the fluid eventually overturned. Javam et al. [37] performed numerical studies on interacting internal waves and confirmed that if harmonic energy could not leave the interaction region in the form of propagating waves, overturning would ensue. On the other hand, if propagating harmonic waves were formed, the harmonics would have frequencies in accordance with (3), and the stratification would not be destroyed. Numerical studies were also performed by Huang et al. [38] in their study of nonresonant interactions in the atmosphere. The analytical work of Tabaei et al. [24] derives equations predicting the amplitudes of harmonics generated by two colliding internal wave beams assuming weakly nonlinear theory. Their derivations predict that up to six second-order harmonic waves are generated, all at different amplitudes.

This study performs laboratory experiments to visualize the two-dimensional flow field, compare qualitative results to Tabaei et al. [24], and determine the energy partitioned to harmonics, when two nonresonant internal waves collide. As the two waves interact, harmonics are generated within the interaction region and propagate from the interaction site at a new frequency. In particular, the second-harmonics, where A and B in (3) are equal to one, are analyzed. Frequencies of the colliding wave beams are chosen to ensure the harmonic frequencies are not evanescent.

The laboratory setup and analysis techniques are described in §2. Results are presented in §3, and §4 contains conclusions.

2. Methods

2.1. Experimental Setup

Experiments are performed in a 11.4 X 91 X 244 cm acrylic tank which is filled with linearly stratified salt water using the "double bucket" method [39]. The density profile is determined by taking fluid samples at various depths. The density of each fluid sample is measured using an Anton Paar 4100 density meter which is accurate up to 0.1 kg/m^3. The buoyancy frequency is found directly from the density profile and has a typical value of $N = 1.180 \pm 0.005$.

Two internal waves are created using wave generators based on the design of Gostiaux et al. [40]. Each wave generator consists of nine plates manufactured from 0.635 cm thick acrylic which form a single wavelength (Figure 1). The plates are separated by 0.1 cm resulting in a total generator height of 6.5 cm. The plates are 11.2 cm wide, only 0.2 cm less than the width of the tank, to ensure the generated wave is two-dimensional. Traversing through the center of the plates is a cam which is driven by a shaft extending above the water surface to a motor. As the motor turns the cam, the cam forces the acrylic plates to move back and forth horizontally in a sinusoidal profile. The cam has an eccentricity of 1 cm, giving the sinusoidal motion of the plates a peak to peak amplitude of 2 cm. The sinusoidal plate motion generates an internal wave beam that has proven to be highly temporally monochromatic and spatially compact when compared to previous internal wave generation methods [40, 41].

The wave generator is situated at a horizontal distance $20 - 40$cm away from the interaction region. When the waves are initiated from the same side the generator of the wave propagating more horizontal is situated just behind the other generator. Thus the wave with a smaller angle with the horizontal has a further distance to propagate to reach the interaction region resulting in a lower amplitude.

The two-dimensional flow field is visualized using synthetic schlieren as described by Sutherland et al. and Dalziel et al. [42, 43]. All synthetic schlieren image processing is performed using Digiflow. Synthetic schlieren allows the flow field to be visualized by tracking the apparent motion of a random pattern of dots placed behind the tank. The dot pattern is created by printing a random pattern of dots on overhead transparencies. This pattern is then placed over a light source, in this case an luminescent sheet. Areas of extreme contrast are formed where the light passes directly through the transparency compared to where the pattern is printed, making the dots highly visible. A camera (JAI, model CV-M4+CL) is focused on this pattern through the fluid filled tank. Because the refraction of light through water depends on the water's salt concentration, as internal waves cause density perturbations in the water, ρ', the dots appear to move. Such apparent dot motion is captured by the camera. Changes in the squared buoyancy frequency, ΔN^2, can be calculated from the vertical motion of the dots by

$$\Delta \mathrm{N}^2 = \alpha \Delta \mathrm{z}, \tag{4}$$

where ΔN^2 can be related to the changing deinsity of the fluid through (2) such that

$$\Delta N^2 = -\frac{g}{\rho_0}\frac{\partial \rho'}{\partial y} \tag{5}$$

and α is a constant that depends on the width of the tank, the thickness of the tank's wall, and the distance from the pattern to the tank [42]. These measurements are 12 cm, 1.8 cm, and 75 cm, respectively, and are important due to the refraction of light from the illuminated pattern to the camera through these mediums. Based on these measurements, α is found to equal 4.1 $\mathrm{cm}^{-1}\mathrm{s}^{-2}$. From the change in the squared buoyancy frequency field, the horizontal velocity, vertical velocity, displacement, and perturbation density fields can be found using equations found in Sutherland et al. [42]. These equations in relation to estimating the energy of the interaction will be discussed further in the next section.

A total of 8 interaction configurations are analyzed in this study. In configurations 1-4, the primary wave is approaching the interaction region at an angle of 10° from the horizontal and always from the same direction. The secondary wave beam approaches the interaction at an angle of 25° from the horizontal; however, for each configuration the secondary wave beam approaches from a different direction. Figure 2(a) illustrates configurations 1-4 on the x-z plane, where the interaction is centered at the origin. Similarly, in configurations 5-8 the primary wave beam always approaches from the same direction at 15° from the horizontal, and the secondary wave beam approached at 40° but from different directions (Figure 2(b)).

2.2. Energy Analysis

Using the synthetic schlieren method previously described estimates of ΔN^2 are made. To estimate the energy associated with these density variations we assume density pertubations are small and wave solutions are planar. We can then use the Polarization Relations to relate the density perturbation to the vertical velocity field, $v = v_0 \cos(kx + ly - \omega t)$, by

$$\rho'(x, z, t) = -\frac{\rho_0 N^2}{\omega g} v_0 \sin(kx + ly - \omega t) \tag{6}$$

where l is the vertical wavenumber and is defined as $l = k\cot\theta$ and $\theta = \sin^{-1}(\omega/N)$. Taking the time derivative and using the definition of v we find

$$\frac{\partial \rho'}{\partial t} = \frac{\rho_0 N^2}{g} v \tag{7}$$

Differentiating with respect to y and using (5) yields

$$\frac{\partial \Delta N^2}{\partial t} = -N^2 \frac{\partial w}{\partial y} \tag{8}$$

Unfortunately integrating Eq.7 directly for w is difficult as the constants of integration are unknown at the boundaries of the schlieren images. However, following the method of Wunsch and Brandt [15] we can relate the measured ΔN^2 to energy. First we define the velocities and density fields as

$$u(x, y, t) = \int U(k, y, \omega) e^{i(kx+ly-\omega t)} dk d\omega \tag{9}$$

$$v(x, y, t) = \int W(k, y, \omega) e^{i(kx+ly-\omega t)} dk d\omega \tag{10}$$

$$\Delta N^2(x, z, t) = \int \Delta N_0^2(k, z, \omega) e^{i(kx+ly-\omega t)} dk d\omega \tag{11}$$

where U, V, and ΔN_0^2 are the amplitudes of each mode at depth y. Conservation of mass for this system is

$$\partial u/\partial x + \partial v/\partial v = 0 \tag{12}$$

Using (8) and (12) and neglecting derivatives of the amplitudes we Fourier transform the results to find an expression for the kinetic energy

$$|U(k, y, \omega)|^2 + |V(k, y, \omega)|^2 = \frac{\omega^2}{N^2 k^2 (N^2 - \omega^2)} |\Delta N_0^2|^2 \tag{13}$$

	Setup 1 and 3		Setup 2 and 4		Setup 5 and 7		Setup 6 and 8	
	x (m)	y (m)	x (m)	y (m)	x (m)	y (m)	x (m)	y (m)
Vertex 1	0	0	0	0	0	0	0	0
Vertex 2	0.465	-0.065	0.190	0.095	0.260	-0.055	0.120	0.110
Vertex 3	0.850	-0.240	0.450	0.055	0.480	-0.230	0.280	0.070
Vertex 4	0.385	-0.175	0.260	-0.040	0.220	-0.175	0.160	-0.040

Table 1: Coordinates of vertices to define control volumes. The origin is defined to be at vertex 1 (Figure 3).

To estimate the kinetic energy partitioned to the harmonic frequencies as a result of the interaction, a control volume is created around the interaction. The energy in each frequency that crosses the control volume's boundaries is then analyzed. Although a variety of control volume shapes and sizes were tested, a control volume tightly around the interaction region in the shape of a parallelogram, as illustrated in figure 3, proves to be the most useful. This figure depicts the ΔN^2 field and the crests and troughs of the internal waves are visible as the darker and lighter shades. The control volume shown around where the two waves meet is preferable because it borders the interaction region equidistant on all sides and isolates the incoming energy from the primary and secondary wave beams across single control volume boundaries. The control volumes' exact size and shape are dependent on the interaction region for each configuration. Thus the size and volume of each control volume may vary; although, each control volume takes the form of a parallelogram. The uncertainty associated with the exact placement of the control volumes around the interaction region was less than 3%.

Due to symmetry the control volume for configurations 1 and 3 is exactly the same size and shape. Likewise, the control volume is exactly the same for configurations 2 and 4. Figure 3 labels the four vertices that make up the control volume for configurations 1-4. Configurations 5-8 have similar control volumes. Defining vertex 1 to be the origin, Table 1 defines the control volumes' vertices for all 8 configurations.

To estimate the energy coming through each of the control volume's four boundaries, a time-series was created for each control volume boundary. Knowing that the only energy entering the control volume is from the primary and secondary waves which are entering at known frequencies and boundaries, the energy entering and leaving the control volume can be determined in Fourier space. Peaks at each harmonic frequency reveal energy partitioned to the harmonics. Then the difference between the total energy entering and exiting the control volume results in an estimate of the total energy dissipated within the interaction region using (13).

3. Results

3.1. Qualitative Observations

Figure 3(b) depicts the spatial flow field of two colliding waves positioned in configuration 4, where the primary wave beam is coming from the top left and the secondary wave beam is coming from the bottom left. The wavefield has reached a steady state. The primary wave beam approaches at a shallower angle to the horizontal than the secondary. It also has less energy associated with it due to the initial location of the wave generator being further from the interaction region. The exiting primary and secondary wave beams can be seen to the right of the interaction. Notice the slight presence of a harmonic on the right of the interaction as well, just between the exiting primary and secondary wave beams. The parallelogram circumscribes the interaction region.

Second harmonics are clearly visible after using a bandpass filter to view the flow fields of the harmonic frequencies. Figure 4(a) shows the ΔN^2 field for the harmonic frequencies equal to the difference of the primary and secondary frequencies, and Figure 4(b) displays their sum. As expected, the harmonic beams appear to be generated within the interaction region, which is enclosed by the solid lines. The dashed lines are locations of harmonic waves predicted by Tabaei et al. [24] that are visible. The dotted lines are locations of harmonic waves predicted by Tabaei et al. that are not seen here. Tabaei et al. [24] predict for this case that two difference harmonics ($\omega_{harmonic} =\mid \omega_1 - \omega_2 \mid$) and four sum harmonics ($\omega_{harmonic} =\mid \omega_1 + \omega_2 \mid$) will be generated.

An initial inspection of the difference harmonic results in Figure 4(a) may indicate that four harmonic beams are propagating away from the interaction, in the form of the St Andrew's Cross, and that these results contradict those by Tabaei et al. However, examining the phase propagation of the harmonic field over time reveals that the two harmonic beams seemingly propagating leftward, away from the interaction site, are actually propagating toward the interaction and must be traces of the harmonic frequency found in the approaching primary and secondary waves. This is possible considering the generation mechanism of the colliding waves creates harmonics due to the oscillating source [41]. The only difference harmonic frequency beams that are indeed being generated within the interaction site are heading rightward, away from the interaction, in accordance with predictions by Tabaei et al., as signified by the dashed lines.

The harmonics have varying amplitudes which are a function of the incoming wavebeam amplitudes as shown by Tabaei et al. [24]. The horizontal and vertical wavelength structure of the harmonics can also be seen and is of the same order as the incoming wavebeams.

Filtered harmonic fields for the remaining configurations are also qualitatively compared to prediction by Tabaei et al. [24]. Considering the center of the interaction to be the origin of the two-dimensional interaction, Table 2 shows in which quadrant second-harmonics can be seen propagating away from the interaction for configurations 1-4. A "yes" in the table denotes harmonics were seen in the experiments and were expected by Tabaei et al. A "no" represents a situation where a wave was predicted by Tabaei et al. but it was not seen in these experiments. Just because a harmonic is not seen qualitatively does not necessarily indicate it does not exist, it is just not captured by this visualization mechanism. No harmonics were seen propagating where Tabaei et al. did not expect them, which is shown by ' – ' in the table. Tabaei et al. also found only some of the harmonics expected were visible in their model. Here the same harmonics are seen, in addition to a further harmonic in quadrant 2 of configuration 4. Configurations 5-8 have the same harmonics visible as configurations 1-4.

	Quadrant 1	Quadrant 2	Quadrant 3	Quadrant 4
Configuration 1				
$\mid \omega_1 + \omega_2 \mid$	No	–	–	No
$\mid \omega_1 - \omega_2 \mid$	Yes	No	No	No
Configuration 2				
$\mid \omega_1 + \omega_2 \mid$	No	No	No	No
$\mid \omega_1 - \omega_2 \mid$	–	No	Yes	–
Configuration 3				
$\mid \omega_1 + \omega_2 \mid$	–	Yes	No	–
$\mid \omega_1 - \omega_2 \mid$	No	Yes	Yes	No
Configuration 4				
$\mid \omega_1 + \omega_2 \mid$	Yes	Yes	No	No
$\mid \omega_1 - \omega_2 \mid$	Yes	–	–	Yes

Table 2: Indication of whether a harmonic was seen propagating away from the interaction within the two-dimensional quadrants, where the origin is at the center of the interaction, for configurations 1-4. ‘ – ’ indicates no harmonic is predicted to be present by Tabaei et al. [24]. Configurations 5-8 were identical.

3.2. Quantitative Energy Analysis

By using the control volume formed around the interaction in Figure 3(b) according to the guide in §2.2, the energy entering and exiting the interaction may be found. By knowing the frequencies of the wave beams approaching the interaction site, the energy of these frequencies may be filtered from the timeseries of the boundaries in which they enter the control volume. An energy spectrum of the total incoming energy for the interaction in Figure 3(b) is shown in Figure 5(a). This represents energy crossing the two left legs of the parallelogram near the primary and secondary wave frequency, and is normalized by the total incoming energy at these frequencies. The two spikes in the energy spectrum represent the energy within the frequencies of the two colliding waves, the primary at the higher frequency and the secondary at the lower. The energy plotted is normalized by the total incoming energy and the frequency is normalized by the buoyancy frequency, $\hat{\omega} = \omega/N$. It is assumed that all other energy passing all four boundaries of the control volume is outgoing and is summed and plotted in Figure 5(b). Here the energy within the difference and sum harmonic frequencies become visible at approximately $\hat{\omega}$ =0.22 and 0.58 respectively.

The energy within the sum and difference harmonic frequencies for all the experiments performed are combined on one plot and presented in Figure 6. The error bars represent the statistical 95% confidence interval of the mean for each interaction configuration, which includes $15 - 20$ tests. Figures 6(a), 6(b) and 6(c) depict the sum, difference, and second sum ($|2\omega_1 + \omega_2|$) harmonics, respectively. Findings show that energy partitioned to the harmonic frequencies is $6 - 19\%$ of the total energy entering the interaction. In these plots it is seen that the sum harmonics generated generally contain significantly more energy than the difference harmonics. The configurations where the colliding waves approach from opposite vertical directions (configurations 3, 4, 7, and 8) partition a much larger portion energy to the sum harmonics.

The energy partitioned to the difference harmonics in configurations 5-8 follows the trend found in configurations 1-4. The difference harmonics extract the most energy when the waves are propagating in opposite vertical directions (configurations 3, 4, 7, and 8) and seems to be independent of the frequencies of the colliding waves.

The second sum harmonic is only possible for configurations 1-4 as the resultant frequency is greater than N for configurations 5-8. Energy in this harmonic is $2-3\%$. The trend of more energy is that configurations 2 and 4, or those propagating opposite horizontal but same vertical directions or propagating same horizontal but opposite vertical directions, are those with the most energy partitioned to the second sum harmonic. A finite amplitude was captured for this harmonic by Tabaei et al. as well.

Figure 7 illustrates an estimated outcome of all energy entering the interaction. Energy which leaves the boundaries of the control volume at the colliding wave primary frequency (the bottom column filled with angled lines) accounts for $5-10\%$ of the energy leaving the interaction. Energy at the colliding wave secondary frequency (gray) accounts for $30-65\%$ of the energy leaving the interaction. Although this partion seems unbalanced, recall in figure 5 that there is significantly more energy coming into the interaction at the secondary wave frequency as well. This is true for all of the interactions.

The energy in the sum harmonic (filled with angled lines) accounts for near 10% of the energy leaving the interaction. The energy in the difference harmonic (dark gray) is only a few percent, and the energy in the second sum harmonic is visible as a few percent in configurations 1-4.

Although much of the energy contained within the primary and secondary colliding waves leaves in these same waves, a significant amount of energy is partitioned to the harmonic frequencies. The energy at these frequencies is due to nonlinear interactions between the colliding waves. The odd numbered configurations have considerably less energy exiting than the other configurations, presumably due to the larger region that the interaction covers and the possibility of dissipation within the interaction region. Again, configurations 3, 4, 7, and 8 are seen to partition a larger portion of energy to the second-harmonics.

4. Conclusions

Laboratory experiments were performed on nonresonant interacting internal waves for 8 unique interaction configurations. Second-harmonics were seen being generated within the interaction region and propagating away. The laboratory experiments support predictions by Tabaei et al. [24]. Although not all predicted harmonics were visible, it is expected that some of them are of such small amplitude they will not be captured (and were not in the model as well). An energy analysis revealed that between $7-19\%$ of the energy entering the interaction is partitioned to the second-harmonics, depending on the configuration. The strongest harmonics were produced when colliding waves approach each other from opposite vertical directions, and here the greatest energy was in the sum harmonic. A repeating trend between configurations 1-4 and 5-8 indicates that the relative quadrants that the waves approach each other from has far more influence on the energy partition to the harmonics than the relative frequencies of the colliding waves. Sum harmonics contain the most energy, and this value can be significant, $10 - 15\%$ of the incoming energy. It is expected that further tests at varying frequencies would yield similar results. A comparison with the theory proposed by Tabaei et al. [24] would complement further experiments.

References

[1] Munk, W., and Wunsch, C., 1998. "Abyssal recipes II: energetic of tidal and wind mixing." *Deep-Sea Research*(45), 1977–2010.

[2] Lamb, K. G., 1994. "Numerical experiments of internal wave generation by strong tidal flow across a finite amplitude bank edge." *Journal of Geophysical Research,* **99**(C1), 843–864.

[3] Garrett, C., 2003. "Internal tides and ocean mixing." *Science (New York, N.Y.),* **301**(5641), 1858–9.

[4] Kim, Y., Eckermann, S. D., and Chun, H., 2003. "An overview of the past, present and future of gravitywave drag parametrization for numerical climate and weather prediction models." *Atmosphere-Ocean,* **41**(1), 65–98.

[5] Godoy-Diana, R., Chomaz, J.-M., and Donnadieu, C., 2006. "Internal gravity waves in a dipolar wind: a wavevortex interaction experiment in a stratified fluid." *Journal of Fluid Mechanics,* **548**, 281–308.

[6] Vanderhoff, J. C., and Blackhurst, T. D., 2012. "Numerical investigation of co- and counter-propagating internal wave-vortex interactions." *International Journal of Dynamics of Fluids,* **8**, 69–90.

[7] Brown, S. N., and Stewartson, K., 1980. "On the nonlinear reflexion of a gravity wave at a critical level: Part 1." *J. Fluid Mech.,* **100**, 577–595.

[8] Thorpe, S. A., 1981. "An experimental study of critical layers." *J. Fluid Mech.,* **103**, 321–344.

[9] Winters, K. B., and D'Asaro, E. A., 1989. "Two-dimensional instability of finite amplitude internal gravity waves packets near a critical layer." *J. Geophys. Res.,* **94**, 12,709–12,719.

[10] Winters, K. B., and Riley, J. J., 1992. "Instability of internal waves near a critical level." *Dyn. Atmos. Oceans,* **16**, 249–278.

[11] Winters, K. B., and D'Asaro, E. A., 1994. "Three-dimensional wave instability near a critical level." *J. Fluid Mech.,* **272**, 255–284.

[12] Delisi, D. P., and Orlanski, I., 1975. "On the role of density jumps in the reflexion and breaking of internal gravity waves." *J. Fluid Mech.,* **69**, 445–464.

[13] Thorpe, S. A., 1998. "Nonlinear reflection of internal waves at a density discontinuity at the base of a mixed layer." *J. Physical Ocean.,* **28** 1853–1860.

[14] Mathur, M., and Peacock, T., 2009. "Internal wave beam propagation in non-uniform stratifications." *Journal of Fluid Mechanics,* **639**, 133–152.

[15] Wunsch, S., and Brandt, A., 2012. "Laboratory experiments on internal wave interactions with a pycnocline." *Expts. in Fluids,* **53**, 1663–1679.

[16] Gregory, K., and Sutherland, B., 2010. "Transmission and reflection of internal wave beams." *Physics of Fluids,* **22**.

[17] Gerkema, T., 2006. "Internal-wave reflection from uniform slopes: higher harmonics and Coriolis effects." *Nonlinear Processes in Geophysics,* **13**(3), 265–273.

[18] Sun, H., and Kunze, E., 1999. "Internal wave-wave interactions. Part I: The role of internal wave vertical divergence." *J. Phys. Oceanogr.,* **29** 2886–2904.

[19] Sun, H., and Kunze, E., 1999. "Internal wave-wave interactions. Part II: Spectral energy transfer and turbulence production." *J. Phys. Oceanogr.,* **29**, 2905–2919.

[20] Walterscheid, R. L., 2000. "Propagation of small-scale gravity waves through large-scale internal-wave fields: Eikonal effects at low-frequency-approximation critical levels." *J. Geophys. Res,* **105**, 18,027–18,037.

[21] Vanderhoff, J. C., Nomura, K. K., Rottman, J. W., and Macaskill, C., 2008. "Doppler spreading of internal gravity waves by an inertia-wave packet." *J. Geophys. Res.,* **113** C05018, doi:10.1029/2007JC004390.

[22] Vanderhoff, J. C., Rottman, J. W., and Broutman, D., 2010. "The trapping and detrapping of short internal waves by an inertia wave." *Physics of Fluids,* **22**.

[23] Crockett, J., and Casaday, B., 2012. "Investigation of high-frequency internal wave interactions with an enveloped inertia wave." *International Journal of Geophysics,* **2012**.

[24] Tabaei, A., Akylas, T. R., and Lamb, K., 2005. "Nonlinear effects in reflecting and colliding internal wave beams." *Journal of Fluid Mechanics,* **526**, 217–243.

[25] Peacock, T., and Tabaei, A., 2005. "Visualization of nonlinear effects in reflecting internal wave beams." *Physics of Fluids,* **17**(6), 061702.

[26] Rodenborn, B., Kiefer, D., Zhang, H. P., and Swinney, H. L., 2011. "Harmonic generation by reflecting internal waves." *Physics of Fluids,* **23**.

[27] Gerkema, T., Staquet, C., and Bouruetaubertot, P., 2006. "Non-linear effects in internal-tide beams, and mixing." *Ocean Modelling,* **12**(3-4), 302–318.

[28] Phillips, O. M., 1960. "On the dynamics of unsteady gravity waves of finite amplitude." *Journal of Fluid Mechanics,* **9**, 193–217.

[29] Martin, S., Simmons, W. F., and Wunsck, C. I., 1969. "Resonant internal wave interactions." *Nature,* **224**, 1014–1016.

[30] McComas, C. H., and Bretherton, F. P., 1977. "Resonant interaction of oceanic internal waves." *J. Geophys. Res.,* **82**, 1397–1412.

[31] Muller, P., Holloway, G., Henyey, F., and Pomphrey, N., 1986. "Nonlinear Interactions Among Internal Gravity Waves." *Reviews of Geophysics,* **24**(3), 493–536.

[32] Staquet, C., and Sommeria, J., 2002. "Internal Gravity Waves: From Instabilities to Turbulence." *Annual Review of Fluid Mechanics,* **34**, 559–593.

[33] Garrett, C., and Munk, W., 1975. "Space-time scales of internal waves: A progress report." *Journal of Geophysical Research,* **80**(3),. 291–297.

[34] McEwan, A., 1973. "Interactions between internal gravity waves and their traumatic effect on a continuous stratification." *Boundary-Layer Meteorology,* **5**(1), 159–175.

[35] Chashechkin, Y., and Neklyudov, V., 1990. "Nonlinear interaction of bundles of short twodimensional monochromatic internal waves in an exponentially stratified liquid." *Dokl. Earth Sci. Sect,* **311**, 235–238.

[36] Teoh, S., Ivey, G., and Imberger, J., 1997. "Laboratory study of the interaction between two internal wave rays." *Journal of Fluid Mechanics,* **336**, 91–122.

[37] Javam, A., Imberger, J., and Armfield, S., 2000. "Numerical study of internal wavewave interactions in a stratified fluid." *Journal of Fluid Mechanics,* **415**(1), 65–87.

[38] Ming Huang, K., Dong Zhang, S., and Yi, F., 2011. "Atmospheric gravity wave excitation through sum nonresonant interaction." *Journal of Atmospheric and Solar-Terrestrial Physics,* **73**(17-18), 2429–2436.

[39] Oster, G., 1965. "Density Gradients." *Scientific American,* **213**, 70–76.

[40] Gostiaux, L., Didelle, H., and Mercier, S., 2007. "A novel internal waves generator." *Experiments in fluids,* **42**, 123–130.

[41] Mercier, M., Martanand, D., Mathur, M., Gostiaux, L., Peacock, T., and Dauxois, T., 2010. "New wave generation." *Journal of Fluid Mechanics,* **657**, 308–334.

[42] Sutherland, B. R., Dalziel, S. B., Hughes, G. O., and Linden, P. F., 1999. "Visualization and measurement of internal waves by synthetic schlieren. Part 1. Vertically oscillating cylinder." *Journal of Fluid Mechanics,* **390**, 93–126.

[43] Dalziel, S. B., Hughes, G. O., and Sutherland, B. R., 2000. "Whole-field density measurements by 'synthetic schlieren'." *Experiments in Fluids,* **28**(4), 322–335.

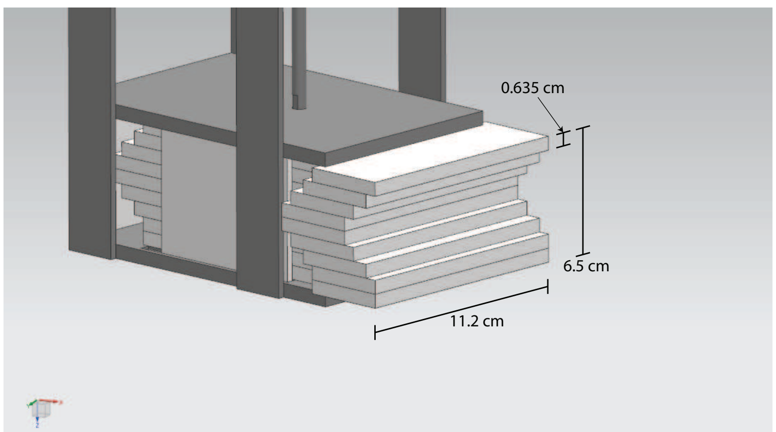

Figure 1: Wave generator consisting of 9 acrylic plates. A rotating shaft extends into a cam through the center of the plates. The cam causes the plates to move in a sinusoid profile, generating an internal wave beam.

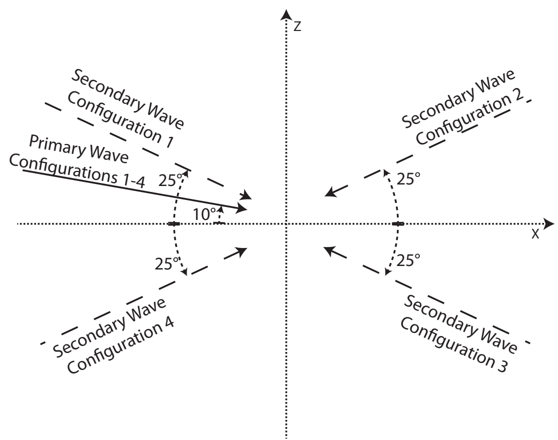

(a) Configurations 1-4

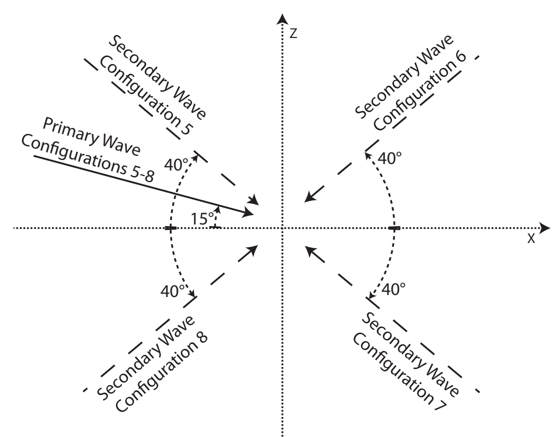

(b) Configurations 5-8

Figure 2: Wave interaction setups for all 8 configurations, where the origin is the interaction location. For configurations 1-4 (a) the primary wave is approaching the interaction at 15° from the horizontal and always from the same direction. The secondary wave always approaches at 25° from the horizontal but from different directions for each configuration as labeled. Configurations 5-8 are similar as shown in (b).

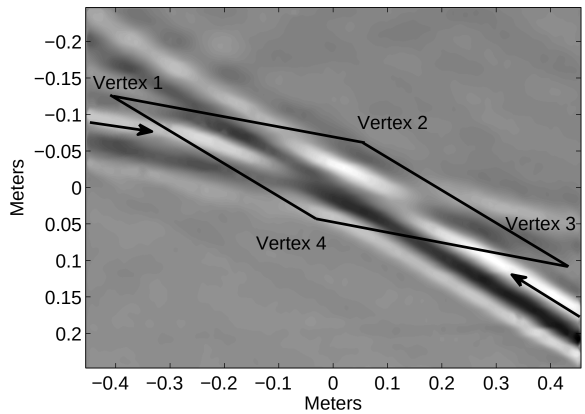

(a) Control volume for configurations 1 and 3

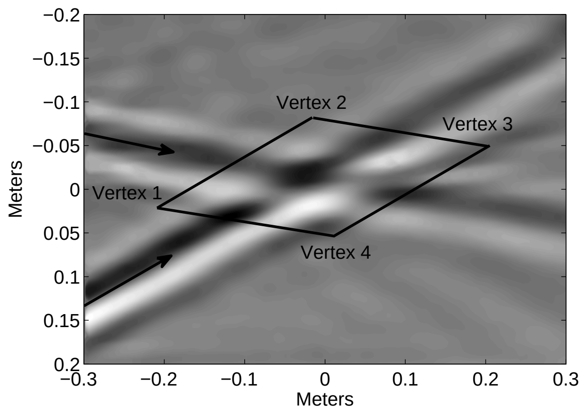

(b) Control volume for configurations 2 and 4

Figure 3: ΔN^2 fields for configurations (a) 1 and 3 and (b) 2 and 4. Vertical axis corresponds to the vertical (y) in the tank and horizontal is along the tank (x). Lines represent control volumes around the interaction region. Control volume vertices are labeled.

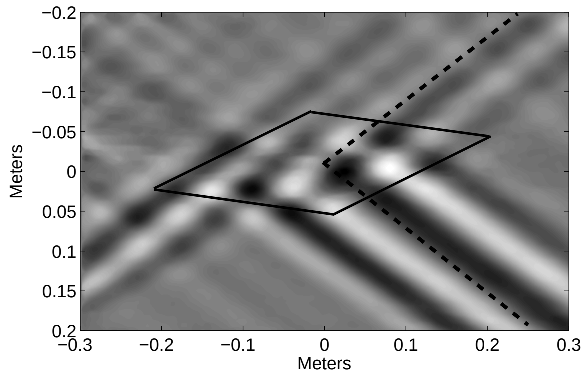

(a) Difference harmonic frequency flow field

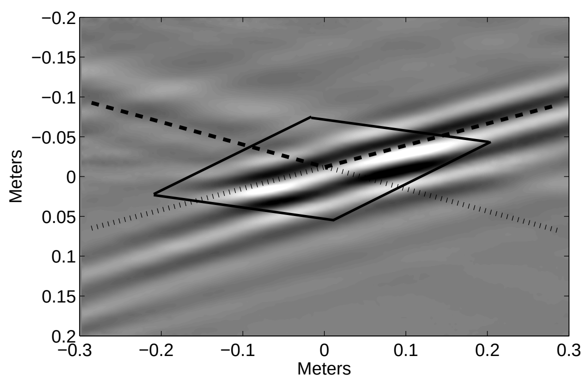

(b) Sum harmonic frequency flow field

Figure 4: Interaction flow field of configuration 4 filtered for (a) the difference harmonic frequency and (b) sum harmonic frequency. Enclosed solid lines represent the interaction region of the two colliding waves. The dashed lines are locations of harmonic waves predicted by Tabaei et al. [24] that are visible. The dotted lines are locations of harmonic waves predicted by Tabaei et al. that are not seen here.

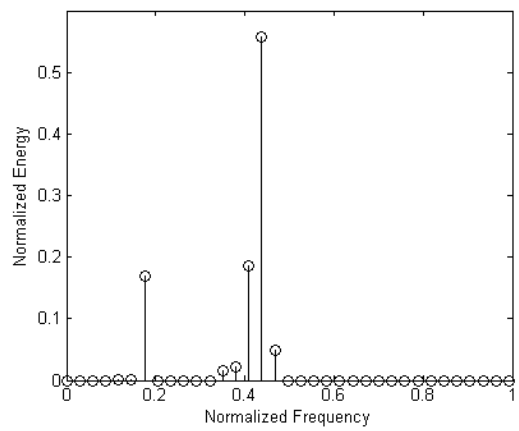

(a) Incoming Energy

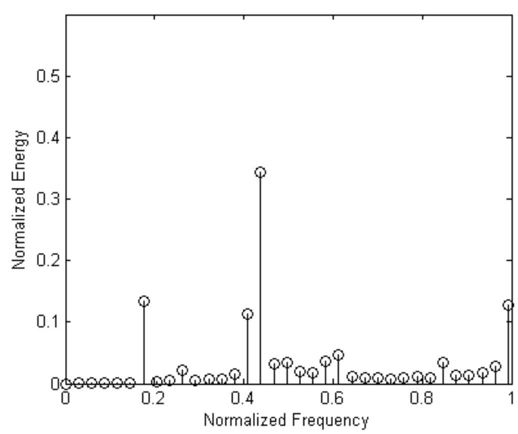

(b) Outgoing Energy

Figure 5: Energy spectrums of incoming (a) and outgoing (b) energy for the interaction in Figure 3(b).

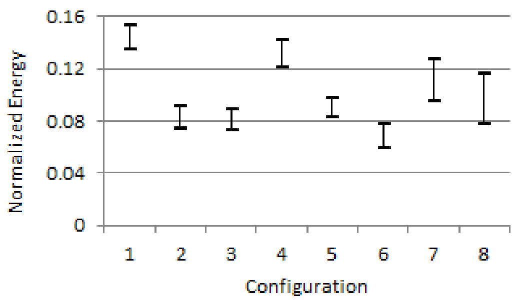

(a) Sum harmonic energy partition

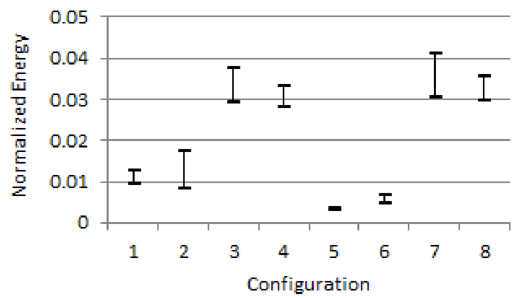

(b) Difference harmonic energy partition

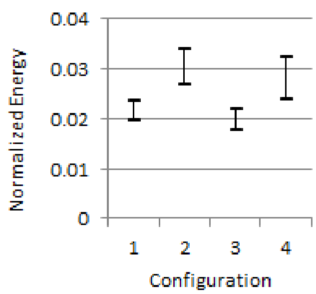

(c) Second sum harmonic energy partition

Figure 6: Normalized energy partitioned to (a) the sum harmonic, (b) the difference harmonic, and (c) the second sum harmonic ($2\omega_1 + \omega_2$). Error bars represent the statistical 95 % confidence interval of the mean.

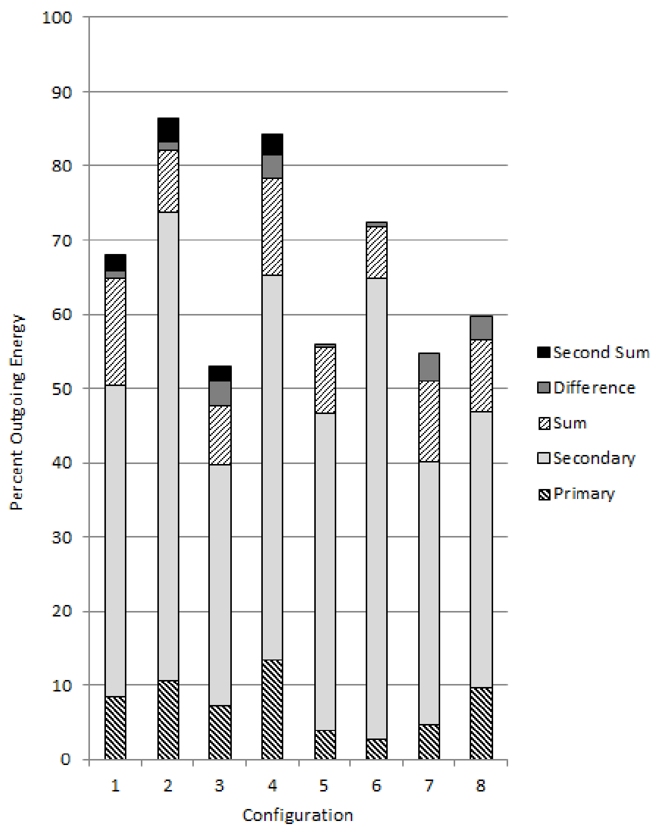

Figure 7: Percentage of captured energy (normalized by the incoming energy of the primary and secondary waves) after the interaction partitioned to the primary, secondary, sum harmonic, difference harmonic, and second sum harmonic as shown in the legend for each configuration.